

Using an Atomically Thin Layer of Hexagonal Boron Nitride to Separate Bound Charge-Transfer Excitons at Organic Interfaces

Shanika Wanigasekara,¹ Kushal Rijal^{ID},¹ Fatimah Rudayni,^{1,2} Mohan Panth,¹ Andrew Shultz,¹ Judy Z. Wu^{ID},¹ and Wai-Lun Chan^{ID}^{1,*}

¹*Department of Physics and Astronomy, University of Kansas, Lawrence, Kansas 66045, USA*

²*Department of Physics, Jazan University, Jazan 45142, Saudi Arabia*



(Received 22 April 2022; revised 31 May 2022; accepted 17 June 2022; published 18 July 2022)

We successfully use two-dimensional hexagonal boron nitride (*h*-BN) as a continuous and ultrathin insulator to facilitate the conversion of excitons into free carriers at organic donor-acceptor (*D*-*A*) interfaces. Monolayer- (0.33 nm) thick *h*-BN with a lateral size on the order of 1 cm² is inserted between zinc phthalocyanine (ZnPc) and perylenetetracarboxylic diimide (PTCDI) organic films that form a generic *D*-*A* interface. We find that *h*-BN increases the photon-to-free-carrier conversion yield of the *D*-*A* heterostructure by 130% compared with identical samples without a *h*-BN layer, even though *h*-BN lowers the initial electron-transfer rate from ZnPc to PTCDI. The enhanced photon-to-free-carrier conversion yield is attributed to a larger charge-separation yield of charge-transfer (CT) excitons at the *D*-*A* interface. *h*-BN can prohibit the formation of tightly bound CT excitons and impede electron-hole recombination, which can improve the charge-separation yield.

DOI: 10.1103/PhysRevApplied.18.014042

I. INTRODUCTION

Exciton dissociation is a critical process for converting photons into free carriers in organic photovoltaic (OPV) and optoelectronic devices. At a typical organic donor-accepter (*D*-*A*) interface, the electron and hole, separated by the *D*-*A* interface, remain bound together by their Columbic interaction. This bound electron-hole pair is known as a charge-transfer (CT) exciton [1–5]. The binding energy of the CT exciton increases with a decrease in the electron-hole separation, and it can reach as high as about 0.5 eV when the electron and hole are localized next to each other at the *D*-*A* interface [6,7]. Thermodynamically, these tightly bound CT excitons mostly recombine, unless an *E* field is present near the interface to assist the separation of the CT exciton and to sweep out the separated charges. Hence, a large energy loss is often required to achieve a high charge-separation (CS) yield. This energy loss is identified as a major factor that limits the open-circuit voltage and OPV efficiency [8–10]. One of the strategies to increase the CS yield is to avoid the formation of these tightly bound CT excitons. This can be achieved, for instance, by inserting a molecularly thin insulating layer at the *D*-*A* interface, which spatially separates donor and acceptor molecules, and hence, lowers the CT-exciton binding energy. The insulating layer can further

improve the CS yield by suppressing both geminate and nongeminate recombination.

However, implementing this strategy with traditional thin-film materials can be very challenging. Previously, wide-band-gap organic molecules [11] or ionic compounds such as LiF [12] were used. These materials unavoidably mix with donor or acceptor molecules at the *D*-*A* interface physically *via* diffusion. Interlayer mixing makes the thin insulating barrier spatially nonuniform, on which bound CT excitons can still form readily in some porous areas. To form a continuous and effective insulating barrier, a thicker insulating layer is often needed. However, a thicker interlayer significantly impedes CT between donor and acceptor molecules. When the interfacial CT process is impeded, the CT exciton cannot be formed in the first place. Because of this trade-off, there has been limited success in using this strategy to improve the CS yield. Even for some successful demonstrations, the insulating layer can only incrementally improve the OPV efficiency within a very narrow window of the insulating-layer thickness (\sim 0.5–1 nm) [11]. In addition, the nonideal interlayer can lower the efficiency, compared with similar devices without the insulating layer, when its thickness is either below or above the optimal range.

Compared with traditional thin-film materials, two-dimensional (2D) van der Waals (vdW) materials provide a more viable pathway to control the interfacial structure at the atomic scale. Moreover, the natural compatibility between 2D crystals and organic molecules (both are vdW

*wlchan@ku.edu

materials) has resulted in recent research interest in designing organic 2D hybrid heterostructures for various applications [13–16]. With the maturing of growth and transfer techniques of 2D layered crystals, inserting an atomically thin yet continuous insulating layer between the donor and acceptor layers becomes feasible. For example, we recently developed a dry transfer method for transferring cm-sized continuous graphene onto organic films without immersing the organic layer in any solvents [17]. This scalable method can, in principle, be used to transfer other 2D crystals as well. In this work, we use this method to transfer monolayer (ML) hexagonal boron nitride (*h*-BN) onto an organic thin film. ML *h*-BN is one of the thinnest (0.33 nm) yet continuous insulating materials (band gap approximately 6 eV) that one can fabricate [18]. A continuous ultrathin insulator minimizes its adverse impact on the CT process, while effectively weakening CT-exciton binding and reducing the electron-hole recombination rate.

Here, we successfully produce a cm-sized donor/*h*-BN/acceptor multilayer structure. Comparing the samples with and without the *h*-BN interlayer, we find that, although ML *h*-BN reduces the initial CT rate at the *D-A* interface, it increases the ns-transient photon-to-free-carrier conversion yield by about 130% under open-circuit conditions. In other words, the conversion yield is more than doubled after *h*-BN is inserted into the *D-A* interface. The increase in the photon-to-free-carrier conversion yield demonstrates that the *h*-BN interlayer effectively assists the CS process by prohibiting the formation of tightly bound CT excitons and reducing CT-exciton recombination. It can potentially be incorporated into various planar heterostructures [19,20]. Finally, ML *h*-BN is mechanically flexible and optically transparent. Therefore, it is highly suitable for use in ultrathin, flexible, or semitransparent organic devices.

II. EXPERIMENTAL METHODS

A. Organic thin-film deposition

The model *D-A* interface used in this work consists of 3,4,9,10-perylenetetracarboxylic diimide (PTCDI) as the acceptor and zinc phthalocyanine (ZnPc) as the donor. PTCDI (Luminescence Technology, >99%) is deposited on a graphene-on-SiO₂/Si substrate using thermal evaporation in an ultrahigh-vacuum (UHV) chamber with a base pressure of 10⁻⁹ Torr. For some samples, ML *h*-BN is transferred on top of the PTCDI film (see Sec. II B). Then, ZnPc (Luminescence Technology, >99%) is deposited on top of the as-prepared sample. The deposition rates are kept at 0.3–0.4 Å/min and 0.8–1.0 Å/min for PTCDI and ZnPc, respectively. The thickness of the organic film is monitored using a quartz-crystal microbalance.

B. Dry transfer for ML *h*-BN

CVD-grown ML *h*-BN on Cu (purchased from Graphene Supermarket) is used. A polyethylene terephthalate (PET)/silicone stamp is employed to transfer *h*-BN onto the PTCDI film. Similar methods are used to transfer ML graphene [17,21]. First, 1 × 0.5 cm² *h*-BN/Cu is pressed onto the PET/silicone stamp by applying a mild pressure for 1 h. The PET/silicone/*h*-BN/Cu stack is then stored in a high-vacuum (HV) chamber overnight (base pressure approximately 10⁻⁷ Torr) to improve adhesion. Next, the Cu foil is etched away using Cu etchant solution (FeCl₃). Similar to the PMMA-assisted wet transfer method [22], the *h*-BN sample is rinsed and washed repeatedly with hydrochloric acid, ammonium hydroxide solution, and deionized water to remove any contaminants. After these cleaning steps, the PET/silicone/*h*-BN stack is dried with N₂ gas and stored in the HV chamber before use. During the final transfer process, both PTCDI and PET/silicone/*h*-BN are removed from the vacuum chamber for a few minutes, and the PET/silicone/*h*-BN stack is pressed onto the PTCDI surface under ambient conditions. Then, the whole sample is stored inside the HV chamber overnight, which improves the adhesion between *h*-BN and the organic film. The whole sample is then removed from the HV chamber for around 1 min to remove the PET/silicone stamp. After dry transfer, the sample is loaded immediately back into the vacuum system. Before depositing the ZnPc layer, the sample is outgassed inside the UHV deposition chamber at 90 °C overnight.

C. Time-resolved two-photon photoemission spectroscopy (TRTPPE)

The ultrafast CT rate from ZnPc (donor) to PTCDI (acceptor) is measured by TRTPPE. In the TRTPPE measurement, 25-fs pump laser pulses with a photon energy of 1.77 eV, which is smaller than the optical band gap of PTCDI, are used to selectively excite the singlet (*S*₁) exciton of ZnPc. The transient population of the ZnPc *S*₁ exciton is probed by time-delayed 60-fs probe laser pulses with a photon energy of 4.68 eV. The probe pulse ionizes the electron of the *S*₁ exciton. The spectrum (intensity vs electron kinetic energy) for the emitted electrons is measured on a hemispherical electron analyzer (SPECS, Phobos 100). Pump and probe pulses are generated from two noncollinear optical parametric amplifiers (NOPA, Orpheus-N-2H; Orpheus-N-3H, Light Conversion). Both NOPAs are pumped by a Yb:KGW regenerative amplifier running at 125 kHz (Pharos 10 W, Light Conversion). The beam size has a full width at half maximum (FWHM) of 0.8 mm at the sample. During the measurement, the sample is kept in the UHV chamber with a base pressure of 1 × 10⁻¹⁰ Torr.

D. Time-resolved graphene field-effect transistor (TRGFET) measurements

The amount of free charges generated by the CS process are measured optoelectronically by using a GFET charge sensor [23,24]. The multilayer sample, either ZnPc/PTCDI or ZnPc/*h*-BN/PTCDI, is fabricated on top of a 1×1 mm² graphene channel. The source and drain electrodes and the graphene channel are prepattered using shadow masks. During the measurement, the sample is kept in an optical cryostat (base pressure approximately 10^{-6} Torr). The sample is excited by 25-fs laser pulses generated by a NOPA (Light Conversion, Orpheus-N-2H). The laser wavelength is set at 700 nm. The laser repetition rate is reduced to 100 Hz by a built-in pulse picker to ensure that all separated charges produced by a laser pulse recombine prior to arrival of the next laser pulse. The pulse energy is about 340 nJ with a FWHM size of about 1.2 mm. The laser-beam size is much larger than the grain size of our organic films, which is on the order of 1–10 μm [25]. Hence, our measurement probes the average property of the whole film and is not affected by local variations in the film thickness originating from the surface or interface roughness. At 700 nm, photons are primarily absorbed by the topmost ZnPc layer. A portion of separated electrons generated by the CS process, which survive recombination events, can transfer to graphene. Charge injection, in turn, induces a conductivity change in the graphene channel. The conductivity change as a function of time is captured by a 200-MHz oscilloscope (Keysight DSOX2024A). In some measurements, a voltage is applied to the Si back gate of the GFET sensor to quantify the amount of free carriers generated from the CS process. For time-resolved measurements, graphene is transferred onto a glass substrate (without the back gate) instead of a SiO₂(300 nm)/Si substrate to obtain a better time resolution [23].

III. RESULTS AND DISCUSSION

A number of experimental techniques are used to characterize ZnPc/*h*-BN/PTCDI and ZnPc/PTCDI heterostructures. This section is organized as follows. First, we show results obtained from Raman spectroscopy and ultraviolet photoemission spectroscopy (UPS). These results demonstrate that a continuous layer of *h*-BN can be transferred onto PTCDI, and the presence of *h*-BN does not significantly change the highest occupied molecular orbital (HOMO) level alignment between the ZnPc and PTCDI layers. Second, we discuss the CT dynamics measured by the TRTPPE. It is found that *h*-BN increases the interfacial CT time from 190 to 270 fs. Despite a slower CT time, CT excitons can still form across the *D-A* interface. The overall photon-to-free-carrier conversion yield depends on the CS yield of these CT excitons. In the third part of this section, we show results from the TRGFET experiment, which probes the overall photon-to-free-carrier conversion

yield. It is found that *h*-BN increases the conversion yield by 130%.

A. Characterization of the ZnPc/*h*-BN/PTCDI multilayer structure

Samples consisting of PTCDI, ML *h*-BN, and ZnPc are fabricated on graphene, unless otherwise stated. Figure 1(a) shows a schematic diagram of the layered structure used in this work. ML *h*-BN is transferred onto the PTCDI layer using a dry transfer method that we have developed for transferring graphene [17]. An optical microscope image near the edge of *h*-BN is shown in Fig. 1(b), where a continuous *h*-BN layer can be observed.

To further demonstrate that ML *h*-BN on PTCDI is continuous, transferred *h*-BN is probed by Raman spectroscopy. Raman spectra are recorded with a commercial Raman imaging system (WiTec alpha300) equipped with a 532-nm laser. To avoid confusion of the *h*-BN peak with the graphene *D* peak, the sample used for Raman spectroscopy does not contain an underlying graphene layer. Figure 1(c) shows a pair of Raman spectra recorded for the ZnPc(3 nm)/*h*-BN/PTCDI(5 nm)/SiO₂/Si (red) and ZnPc(3 nm)/PTCDI(5 nm)/SiO₂/Si (blue) samples. For the sample with *h*-BN, an additional peak at 1362 cm⁻¹ is observed [labeled by a star in Fig. 1(c)], which can be attributed to the B-N vibrational mode (*E*_{2g}) of the *h*-BN layer [26]. Other peaks in the spectra can be assigned to the two molecules because all these peaks can be found in samples with and without *h*-BN. Note that the *E*_{2g} peak is located at about 1370 cm⁻¹ when ML *h*-BN is transferred onto the SiO₂/Si substrate [Fig. 1(d)]. The slight shift in the Raman peak position originates from the interaction between *h*-BN and the molecules. Figure 1(e) shows the Raman mapping image for the *h*-BN *E*_{2g} peak. The uniform intensity map indicates that *h*-BN is continuous.

We also perform UPS measurements on transferred *h*-BN. The UPS measurement is done by using the He-I emission line (21.22 eV) generated from a standard UV discharge lamp. Figure 2 shows the UPS spectrum of transferred *h*-BN on PTCDI. The energy axis is referenced with respect to the Fermi level (*E*_F). The spectrum is taken at the Γ point. The σ and π bands of *h*-BN are clearly visible and their energy positions agree well with previous measurements on exfoliated *h*-BN [27]. Because UPS is an extremely surface-sensitive technique, the result indicates that the *h*-BN surface does not have a significant amount of contamination. Focusing on the spectral region near the Fermi level (inset in Fig. 2), the PTCDI HOMO peak can be seen, although its intensity is attenuated compared with spectrum obtained for the bare PTCDI sample (yellow line). Because *h*-BN is continuous, the appearance of the PTCDI HOMO peak shows that the *h*-BN/PTCDI

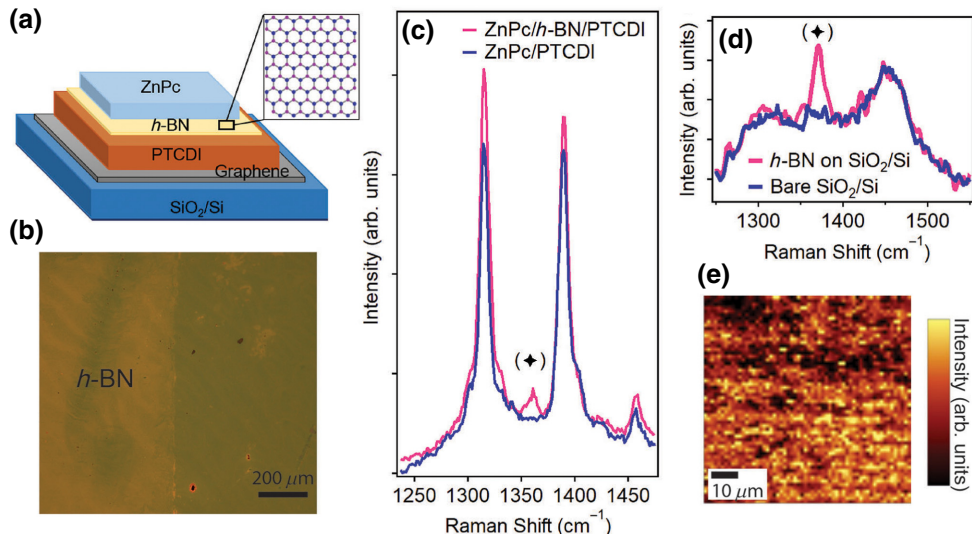


FIG. 1. (a) Schematic diagram showing how the *h*-BN film is sandwiched between donor and accepter layers deposited on graphene/SiO₂/Si. (b) Optical microscope image of ZnPc(3 nm)/*h*-BN/PTCDI(5 nm) sample at the edge of *h*-BN. (c) Comparison of the Raman spectra of ZnPc(3 nm)/*h*-BN/PTCDI(5 nm) (red) and ZnPc(3 nm)/ZnPc/5-nm PTCDI samples (blue). Additional peak at about 1362 cm⁻¹ is ascribed to ML *h*-BN. (d) Comparison of the Raman spectra of *h*-BN transferred onto a SiO₂/Si substrate with bare SiO₂/Si substrate. (e) Raman mapping image of the intensity of the *h*-BN *E*_{2g} phonon mode. Uniform intensity indicates that *h*-BN is continuous.

interface does not have a significant amount of contamination, which would have blocked photoelectrons originating from the underlying PTCDI layer.

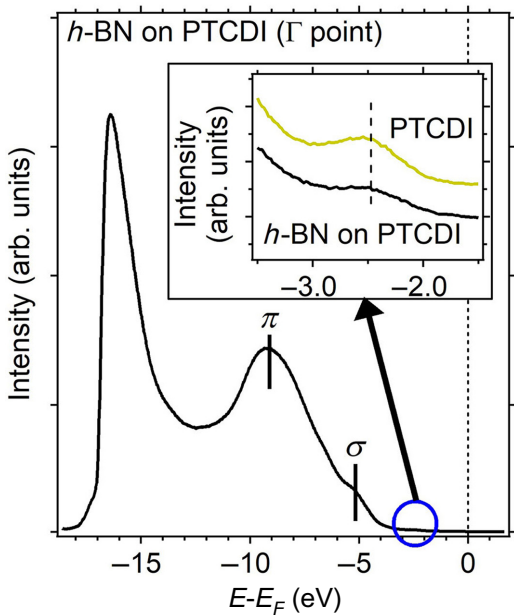


FIG. 2. UPS spectrum of *h*-BN on PTCDI(10 nm) sample. Spectrum is taken at the Γ point. The σ and π bands of *h*-BN are labeled. Region near the Fermi level is magnified and shown in the inset. In the inset, the spectrum is compared with the spectrum recorded for a bare PTCDI(10 nm) sample. PTCDI HOMO is visible in the *h*-BN/PTCDI spectrum.

We further measure the energy-level alignment at the *D-A* interface with UPS. Figures 3(a) and 3(b) show the UPS spectra obtained for PTCDI(10 nm), ZnPc(1 nm)/*h*-BN/PTCDI(10 nm), and ZnPc(10 nm)/*h*-BN/PTCDI(10 nm) samples. We also obtain UPS spectra for ZnPc/PTCDI samples without the *h*-BN interlayer, which are shown as blue lines in Fig. 3. The secondary-electron cutoff (SECO) region of the UPS spectra is shown in Fig. 3(a), while the region near the HOMO peak is shown in Fig. 3(b). The HOMO onsets of PTCDI and ZnPc are indicated by vertical lines in Fig. 3(b), which can then be used to determine the HOMO alignment. The energy-level diagram between PTCDI and ZnPc is shown in Fig. 3(c). The energy axis is referenced with respect to the Fermi level (E_F). The lowest unoccupied molecular orbital (LUMO) position in Fig. 3(c) is determined by using the reported HOMO-LUMO gaps (offset-to-offset) of the two molecules [28,29]. For ZnPc, the HOMO offsets determined from those 1-nm samples are used to produce Fig. 3(c), and the red and blue lines represent the energy levels with and without the *h*-BN interlayer, respectively. In both cases (with and without *h*-BN), ZnPc/PTCDI has a type-II band alignment, and the HOMO offset is not significantly affected by the insertion of the *h*-BN layer.

The ionization potential (IP) of planar molecules, such as ZnPc, depends on the molecule's orientation with respect to the substrate [30–32]. We can use the IP value to determine whether *h*-BN would have changed the orientation of the ZnPc molecule. For ZnPc and similar phthalocyanine molecules, multiple studies have shown that films

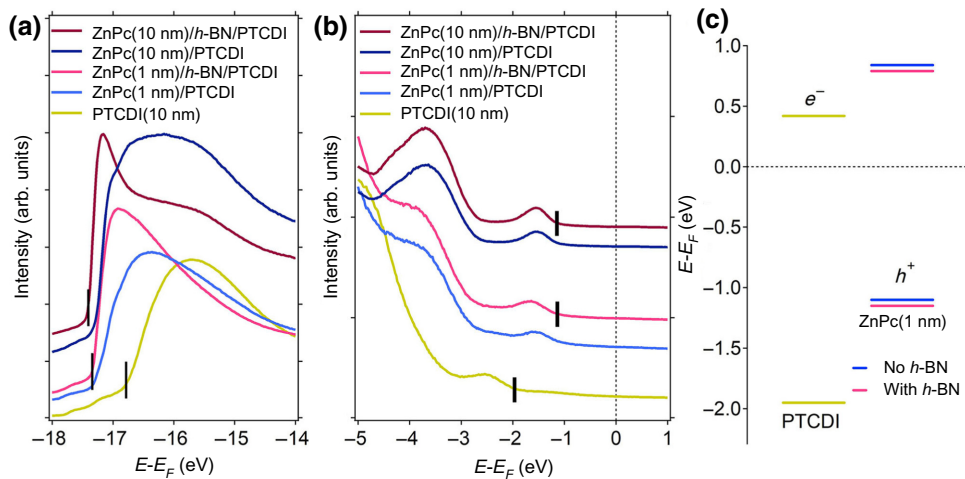


FIG. 3. UPS spectra of a series of samples with different thicknesses that are used to determine HOMO-level alignment at the ZnPc/h-BN/PTCDI interface. Samples used are as follows: PTCDI(10 nm), ZnPc(1 nm)/h-BN/PTCDI(10 nm), and ZnPc(10 nm)/h-BN/PTCDI(10 nm). Two blue lines represent spectra from ZnPc/PTCDI bilayer samples without the *h*-BN layer. Spectral regions (a) near the SECO, and (b) near the HOMO peak are shown. (c) Band alignment of ZnPc/PTCDI determined from the UPS spectra. Red and blue lines represent ZnPc energy levels at interfaces with and without *h*-BN, respectively. LUMO levels are estimated using the HOMO-LUMO gap for the two molecules reported in Refs. [28,29].

with face-on-oriented molecules typically have an IP about 0.5 eV larger than that for films with edge-on-oriented molecules [30–32]. The IP can be determined from the energy separation between the SECO and HOMO onset. For PTCDI(10 nm)/graphene, the IP is 6.39 eV, which agrees well with the reported value for face-on-oriented PTCDI (6.42 eV [28]). The IP for ZnPc, determined from samples with a ZnPc(10 nm) top layer, is 5.03 and 5.01 eV for samples with and without *h*-BN, respectively. The two IPs are similar, which indicates that ZnPc molecules grown on *h*-BN and on PTCDI have similar orientations. The IP for face-on-oriented ZnPc is about 5.1–5.3 eV [25,29,30]. Hence, ZnPc has a primarily face-on orientation, but the slight decrease in IP could originate from a slight tilting of the ZnPc molecule with respect to the substrate. Previous studies also showed that phthalocyanine molecules grown on *h*-BN had a face-on orientation [33,34]. Because *D-A* interfaces with and without *h*-BN have similar energy-level alignments and molecular orientations, a direct comparison between samples with and without the *h*-BN interlayer can be done to determine the effect of *h*-BN on CT and CS processes.

B. Impact of *h*-BN on the CT rate at the *D-A* interface

The *h*-BN interlayer can affect both the CT rate across the *D-A* interface, and the dissociation yield of the CT exciton (i.e., the CS yield). First, we use TRTPPE to determine the initial electron-transfer rate from ZnPc (donor) to PTCDI (acceptor). In this experiment, a 1.77-eV (700-nm) pump beam is used to selectively excite the singlet (*S*₁) exciton in the top ZnPc layer. Then, a time-delayed

4.59-eV (270-nm) probe beam is used to ionize the excited electron from the ZnPc *S*₁ exciton. Samples with different ZnPc thicknesses and those with or without *h*-BN are used. All samples have a PTCDI(10 nm) bottom layer that is grown on graphene. The TPPE spectra near time zero for different samples are shown in Fig. 4(a). The final-state energy of the electron with respect to *E*_F is used for the energy axis. Subtracting the probe photon energy (4.59 eV) from the final-state energy gives the energy of the excited state (known as the intermediate-state energy). As discussed in the Supplemental Material [35], referencing the intermediate-state energy with respect to the ZnPc HOMO-peak energy measured by UPS can give us the transition energy of the exciton. Such a plot is shown as Fig. S1 within the Supplemental Material [35]. In Fig. S1 within the Supplemental Material [35], the peak is located at 1.6–1.7 eV, which can be assigned to the ZnPc *S*₁ exciton [36,37]. We note that similar approaches have been used by others to determine the exciton-transition energy from the time-resolved photoemission spectrum [38].

Before discussing the time-resolved measurements, we note that photoemission is a surface-sensitive process. The electron inelastic mean free path (IMFP) depends on the energy of the emitted electron and the nature of the material. Using the universal curve for organic compounds reported in Ref. [39], the final-state energies in Figs. 4(a) and 4(a), and a mass density of 1.7 g cm⁻³, we find that the IMFP is about 1.6 nm. More recent work on pi-conjugated organic semiconductors shows that the IMFP at an energy about 5 eV above *E*_F is about 3 nm [40]. Our previous study on ZnPc deposited on Au showed that, when the ZnPc thickness was larger than 4 nm, the sub-ps dynamics

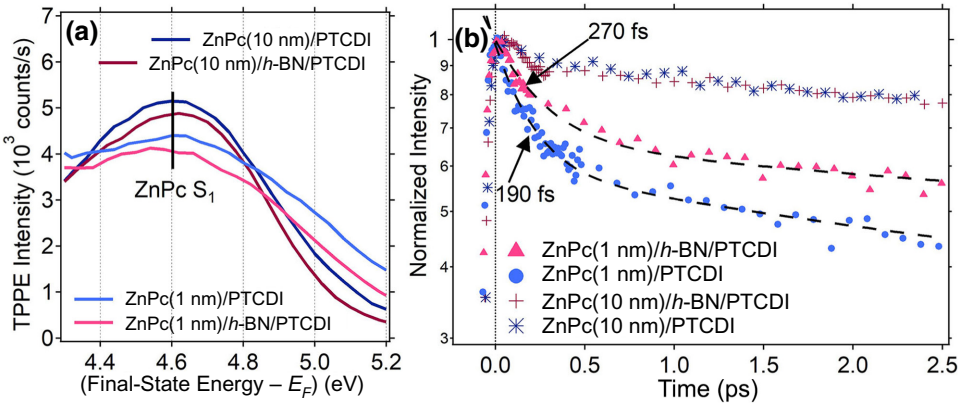


FIG. 4. (a) TPPE spectra for different samples near time zero. Based on our previous works, the peak at about 1.6 eV can be assigned to ZnPc S_1 . (b) Integrated intensity of the ZnPc S_1 peak as a function of time. Intensity near time zero is normalized to one. For the two samples with a ZnPc(1 nm) layer, initial rapid intensity decay results from the CT from ZnPc to PTCDI.

did not change with the film thickness, i.e., the photoemission probe is not sensitive to the CT process at the buried interface for ZnPc films thicker than 4 nm [37]. Our previous measurement [37] implies that the IMFP in our ZnPc films should be less than 4 nm, which is consistent with the reported IMFP for organic materials [39,40]. Hence, in our case, the TPPE probes the ZnPc S_1 exciton located near the surface. We would like to stress that the IMFP is highly dependent on the material in the system. For inorganic materials, the IMFP at low energies can reach up to about 10 nm [39].

Figure 4(b) shows the normalized intensity of the ZnPc S_1 peak as a function of time. Results obtained from the two samples with a ZnPc(10 nm) layer show a rapid intensity decay in the first few hundreds of femtoseconds (fs). For these samples, the S_1 exciton's delocalization size is larger than the ZnPc film thickness [37] and an electron from the S_1 exciton can transfer directly (without the need for slow exciton diffusion) to PTCDI. Hence, the initial rapid signal decay can be primarily attributed to electron transfer from ZnPc to PTCDI, which quenches the signal from the ZnPc S_1 exciton. For the two ZnPc(10 nm) samples, S_1 excitons near the surface cannot diffuse to the ZnPc bottom interface immediately (<1 ps) after photoexcitation [36]. Indeed, for the two 10-nm-thick samples, the intensity decay does not depend on the underlying layers [Fig. 4(b)]. In the Supplemental Material (Fig. S2) [35], we further compare the dynamics of five different ZnPc(10 nm) samples deposited on different substrates. The same sub-ps decay dynamics is observed and is highly reproducible. Hence, we attribute the sub-ps intensity decay of those 10-nm samples to the intrinsic S_1 property of ZnPc, which can originate from processes such as exciton localization or hot-exciton relaxation [37]. For 1-nm samples, the small intrinsic intensity decay from ZnPc convolutes with the population quenching originating from CT to produce the overall intensity decay. Hence, the

convoluted intensity decay rate can systematically overestimate the actual CT rate. However, the extent of this overestimation should be small because the intensity decay originating from CT is much more pronounced than the intensity decay originating from the intrinsic S_1 dynamics.

The dynamics for the two 1 nm samples is fitted with a biexponential decay function (dashed lines). The ZnPc(1 nm)ZnPc/PTCDI sample shows an initial decay time of 190 fs, which is faster than the decay time observed for the 1 nm ZnPc/h-BN/PTCDI sample (270 fs). We note that the decay rates obtained from the TRTPPE experiments are highly reproducible and do not have much sample-to-sample variation. A comparison between data taken from different samples (but with the same thickness) is shown in Fig. S3 in the Supplemental Material [35]. When h-BN is inserted between the donor and the acceptor, CT from ZnPc to PTCDI becomes slower. The h-BN layer spatially separates ZnPc and PTCDI, which reduces the overlap between the two LUMO wave functions, and hence, the CT rate. However, we note that h-BN is thin enough (~ 0.3 nm) so that CT from ZnPc to PTCDI can still occur at a reasonably fast rate (<1 ps).

C. Impact of h-BN on the photon-to-free-carrier conversion yield

The interfacial CT process mentioned in Sec. III B can produce CT excitons at the D - A interface [1–5]. However, these CT excitons are typically bound. To generate free carriers, these CT excitons must undergo successful CS before they recombine. To determine the photon-to-free-carrier conversion yield, we utilize the graphene underlying our samples to probe the number of free charges generated from the CS process. Because graphene's conductivity is highly sensitive to charge doping, the number of separated charges injected into graphene can be quantified by measuring the resistance of the graphene layer,

R_G , as a function of time. The ZnPc-PTCDI heterostructures, with and without the h -BN interlayer, are fabricated on GFET devices. During the measurement, the top ZnPc layer is selectively excited by 700-nm 25-fs laser pulses. For a successful CS event, an electron injects into graphene and the hole remains in the top ZnPc layer. Electron injection creates n doping in graphene, which produces a measurable change in R_G . The change in graphene's channel resistance ($\Delta R_G/R_G$) is captured by a 200-MHz oscilloscope, which is proportional to the number of separated charges after pulse-laser excitation. We previously developed this TRGFET method to probe both the charge-generation dynamics and the charge-generation yield on an organic *D-A* bilayer [23,41] and trilayer [24] and halide perovskite bulk heterostructures [42]. The detailed principle of our method can be found in Ref. [23].

Figures 5(a) and 5(b) show the time-resolved $\Delta R_G/R_G$ signal of a pair of samples, ZnPc(3 nm)/ h -BN/PTCDI (5 nm) and ZnPc(3 nm)/PTCDI(5 nm), on two different timescales. To compare the dynamics, the signal near time zero is normalized to one. The separation of CT excitons produces free charges within the first few ns, which results in the rapid signal rise observed in Fig. 5(a). The instrumental response time of our oscilloscope is about 2 ns, which is shown as the dashed line. The signal decay on

longer timescales is shown in Fig. 5(b), which represents the recombination of separated electron-hole pairs. The recombination time is long because the electron (residing in graphene) and the hole (residing in ZnPc) are separated by the PTCDI(5 nm) layer. We note that the sample with the h -BN layer shows a somewhat slower recombination kinetics compared with the sample without the h -BN layer. This behavior is expected because the h -BN layer spatially separates PTCDI and ZnPc, which reduces the electron-hole recombination rate.

While it is important that h -BN can reduce the recombination of electrons and holes that have already separated, our major goal is to determine whether h -BN would enhance the CS yield of the CT exciton. h -BN can increase the CS yield in three ways. First, it increases the average distance between the electron and hole in the CT exciton, which, in turn, reduces the CT-exciton binding energy. Loosely bound CT excitons should have a faster CS rate because of the lower-energy barrier for CS. Second, h -BN has a slightly larger dielectric constant (~ 6.8 , Ref. [43]) than those of organic materials, and it is known that h -BN can screen free charges from the substrate [44]. Better electronic screening from the environment can lower the exciton-binding energy as well [45]. Third, the h -BN layer reduces the CT-exciton recombination rate by

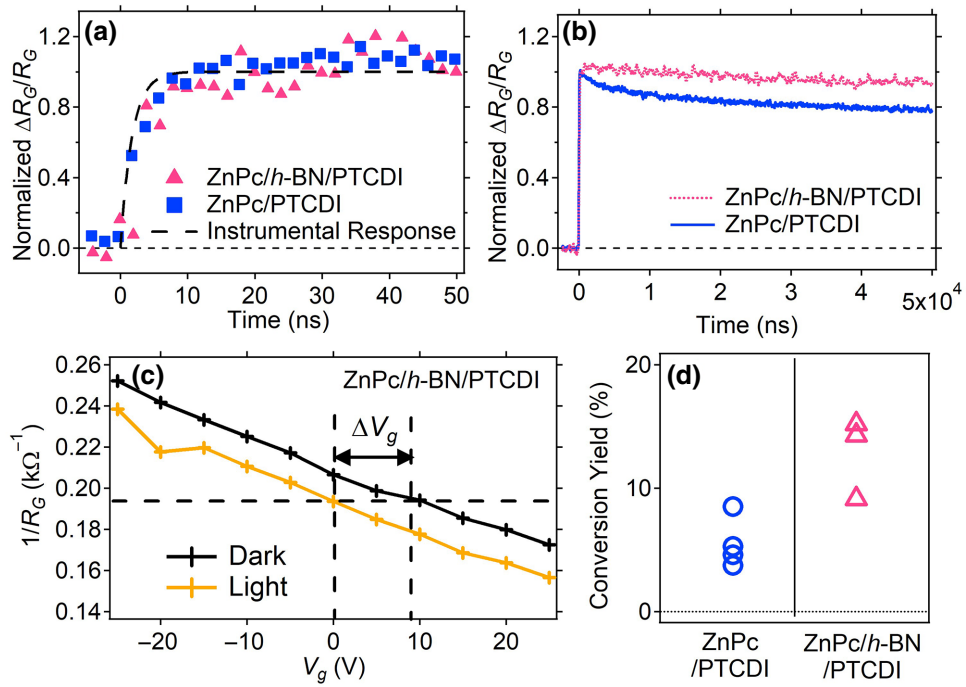


FIG. 5. (a),(b) Normalized $\Delta R_G/R_G$ signal for ZnPc/ h -BN/PTCDI (red) and ZnPc/PTCDI (blue) samples on the ns and μ s timescales. For both samples, the thicknesses for ZnPc and PTCDI are 3 and 5 nm, respectively. (c) Graphene channel conductance ($1/R_G$) as a function of gate voltage (V_g) for ZnPc(3 nm)/ h -BN/PTCDI(5 nm) sample. “Dark” and “light” curves represent conductance before and about 10 ns after arrival of the fs laser pulse, respectively. Horizontal shift of the curve (ΔV_g) can be used to calculate the number of separated charges. (d) Calculated photon-to-free-carrier conversion yield for several independent ZnPc/ h -BN/PTCDI (red) and ZnPc/PTCDI (blue) samples.

reducing the spatial overlap of the electron and hole wave functions. As a result of these three contributions, CT excitons have more time to undergo CS before it recombines. Therefore, the CS yield would be increased by the *h*-BN layer.

The TRGFET experiment is used to measure the photon-to-free-carrier conversion yield, i.e., the number of free charges generated from the heterostructure per absorbed photon. An increase in the photon-to-free-carrier conversion yield can be attributed to an increase in the CS yield. To measure the conversion yield, we use the resistance change (ΔR_G) at $t \approx 10$ ns to determine the number of separated carriers per unit area right after the initial CS process. To correlate ΔR_G with the actual number of separated carriers, back-gated samples with graphene transferred onto SiO₂(300 nm)/Si substrates are used. By applying a back-gate voltage (V_g) to the SiO₂/Si back gate, graphene can be doped electrically and graphene's resistance as a function of V_g can be obtained. Because the number of carriers induced by electrical gating can be determined simply by using the equation of a parallel-plate capacitor, the V_g -dependent measurement can be used to calibrate the response of each individual graphene sensor. A detailed description of this method can be found in our previous work [23]. At each gate voltage, graphene's resistance is determined before ($t < 0$ ns) and immediately after the fs laser pulse excites the sample ($t \approx 10$ ns) by using time traces similar to the one shown in Fig. 5(a). Then, the conductance ($1/R_G$) before (labeled as dark) and after (labeled as light) arrival of the fs laser pulse is plotted as a function of V_g . Figure 5(c) shows an example of these V_g -dependent curves for the ZnPc(3 nm)/*h*-BN/PTCDI(5 nm) sample.

In Fig. 5(c), it is apparent that the whole curve shifts to the left after the arrival of the fs laser pulse. The direction of the shift (to the left) indicates that graphene is doped with additional electrons and holes are trapped in the semiconductor layer (ZnPc in our case) [46]. The number of electrons, N , transferred to graphene after the CS process can be related to the voltage shift (ΔV_g) by the equation for a parallel-plate capacitor [47,48]:

$$N = \Delta V_g \frac{\kappa \epsilon_0 A}{d} \frac{1}{e}, \quad (1)$$

where κ and d are the dielectric constant and thickness of SiO₂, respectively; ϵ_0 is the vacuum permittivity; A is the area of the graphene channel; and e is the electron charge. For our samples, we use $\kappa = 3.6$, $d = 300$ nm, and $A = 1$ mm². Then, the photon-to-free-carrier conversion yield is defined as N divided by the number of absorbed photons. The number of absorbed photons can be estimated by a transfer-matrix model that accounts for the interference effect in the multilayer sample. Details of the transfer-matrix model are described in our previous

publication [23,24] and in the Supplemental Material [35]. In this work, we add the ML *h*-BN layer to our model; the dielectric constant for ML *h*-BN is obtained from Ref. [43]. At 700 nm, most of the optical absorption occurs at the ZnPc layer. To provide a more accurate estimation of the optical absorption, we previously measured the optical extinction coefficient on a series of ZnPc films with different thicknesses [23].

Figure 5(d) shows the calculated conversion yield for samples with and without the *h*-BN layer. For all samples, the thicknesses of ZnPc and PTCDI are fixed at 3 and 5 nm, respectively. In our samples, because graphene is not connected to the ZnPc layer through an external circuit, the separated charges are not extracted from the sample. Hence, our samples are essentially under open-circuit conditions, which can explain the apparently low photon-to-free-carrier conversion yield (<20%). The measured conversion yield represents how much separated charge can be produced transiently on ns timescales after fs-laser-pulse excitation. We note that the laser repetition rate is reduced to 100 Hz to ensure that all these separated charges recombine before the arrival of the next pulse. In Fig. 5(d), each data point represents a measurement from an independent GFET device. We note that the GFET measurement probes the overall charge-conversion yield, which can be sensitive to multiple electronic processes, such as charge transport, trapping, and recombination. The rates of these processes are sensitive to the amount of imperfections in the sample. The device-to-device variations in the conversion yield can originate from imperfections introduced during graphene and *h*-BN transfer. Despite this variation, it is apparent that ZnPc/*h*-BN/PTCDI samples show a larger yield than that of ZnPc/PTCDI samples. The average conversion yield increases from about 5.5% to 12.9% after *h*-BN is added, which represents 130% increase (i.e., the yield is more than doubled). Therefore, we can conclude that *h*-BN improves the CS yield by suppressing the formation of tightly bound CT excitons and various recombination processes.

Finally, we note that *h*-BN slows down all electron-transfer processes between the donor and the acceptor. It may not be apparent that the enhancement in the CS yield can outweigh the reduction in the initial CT rate, which leads to an overall improvement in the photon-to-free-carrier conversion yield. We argue that the initial CT process often involves delocalized states with excess energies [3,7,49,50]. Compared with recombination processes initiated by cold and localized states, the delocalized nature of these hot states would make the initial CT process less susceptible to the increase in the distance between donor and acceptor molecules. Hence, the atomically thin *h*-BN layer should have less impact on the initial CT rate than on the recombination rates. Moreover, the initial CT process at the *D*-*A* interface is very fast (~100 fs) compared with other competing electronic processes. Hence, a slower

CT process would not be detrimental to decreasing the yield for forming CT excitons. By contrast, for the CS process, *h*-BN not only decreases the CT-exciton recombination rate, but it also increases the CS rate by lowering the exciton-binding energy. Both effects can increase the CS yield. According to this understanding, the overall photon-to-free-carrier conversion yield would be further boosted by using two or more *h*-BN layers. However, the yield will decrease drastically when the *h*-BN layer is thick enough to block the initial CT process. The strategy discussed here should also be applicable to other organic *D-A* interfaces.

IV. CONCLUSION

In this work, we demonstrate the use of ML *h*-BN as an ultrathin insulating barrier for enhancing the CS yield of CT excitons at an organic *D-A* interface. Compared with its counterpart of conventional thin-film insulating materials that have been previously used, ML *h*-BN has the advantages of an atomically small thickness of 0.33 nm, negligible mixing at the *D-A* interface, and continuity over a macroscopic area (on the order of cm²). Hence, it can effectively block the formation of tightly bound CT excitons and reduce the recombination of electron-hole pairs across the whole macroscopic interface. The small thickness of ML *h*-BN means that it does not significantly reduce the interfacial CT rate. Specifically, we find that, although ML *h*-BN slows electron transfer from ZnPc to PTCDI (the CT time increases from 190 to 270 fs), it increases the photon-to-free-carrier conversion yield from about 5.5% to 12.9%. In our experiment, the conversion yield is measured under conditions similar to the open-circuit conditions found in PV devices. The enhanced yield under these zero-field conditions implies that a smaller internal *E* field, and hence, a smaller voltage loss, would be needed to produce the photocurrent. Together with the reduction in electron-hole recombination, ML *h*-BN can potentially increase the open-circuit voltage and the fill factor if it is incorporated at the *D-A* interface in ultrathin bilayer or multilayer OPV devices.

ACKNOWLEDGMENTS

This work is supported by US National Science Foundation Grant No. DMR-2109979. Support by the University of Kansas General Research Fund Allocation No. 2151080 is also acknowledged. J.Z.W. acknowledges US National Science Foundation Grants No. NSF-ECCS-1809293 and No. NSF-DMR-1909292 and US Army Grant No. W909MY-21-C-0033. F.R. acknowledges scholarship support from Jazan University.

[1] J. L. Bredas, J. E. Norton, J. Cornil, and V. Coropceanu, Molecular understanding of organic solar cells: The challenges, *Acc. Chem. Res.* **42**, 1691 (2009).

- [2] T. M. Clarke and J. R. Durrant, Charge photogeneration in organic solar cells, *Chem. Rev.* **110**, 6736 (2010).
- [3] A. J. Heeger, 25th anniversary article: Bulk heterojunction solar cells: Understanding the mechanism of operation, *Adv. Mater.* **26**, 10 (2014).
- [4] O. Ostroverkhova, Organic optoelectronic materials: Mechanisms and applications, *Chem. Rev.* **116**, 13279 (2016).
- [5] C. S. Poncea, P. Chabera, J. Uhlig, P. Persson, and V. Sundstrom, Ultrafast electron dynamics in solar energy conversion, *Chem. Rev.* **117**, 10940 (2017).
- [6] X. Y. Zhu, Q. Yang, and M. Muntwiler, Charge-transfer excitons at organic semiconductor surfaces and interfaces, *Acc. Chem. Res.* **42**, 1779 (2009).
- [7] T. Wang, T. R. Kafle, B. Kattel, and W.-L. Chan, A multidimensional view of charge transfer excitons at organic donor–acceptor interfaces, *J. Am. Chem. Soc.* **139**, 4098 (2017).
- [8] J. Z. Yao, T. Kirchartz, M. S. Vezie, M. A. Faist, W. Gong, Z. C. He, H. B. Wu, J. Troughton, T. Watson, D. Bryant, and J. Nelson, Quantifying Losses in Open-Circuit Voltage in Solution-Processable Solar Cells, *Phys. Rev. Appl.* **4**, 014020 (2015).
- [9] B. P. Rand, D. P. Burk, and S. R. Forrest, Offset energies at organic semiconductor heterojunctions and their influence on the open-circuit voltage of thin-film solar cells, *Phys. Rev. B* **75**, 115327 (2007).
- [10] X. Liu, B. P. Rand, and S. R. Forrest, Engineering charge-transfer states for efficient, low-energy-loss organic photovoltaics, *Trends Chem.* **1**, 815 (2019).
- [11] Y. F. Zhong, A. Tada, S. Izawa, K. Hashimoto, and K. Tajima, Enhancement of *V*_{OC} without loss of *J*_{SC} in organic solar cells by modification of donor/acceptor interfaces, *Adv. Energy Mater.* **4**, 1301332 (2014).
- [12] S. Sampat, A. D. Mohite, B. Crone, S. Tretiak, A. V. Malko, A. J. Taylor, and D. A. Yarotski, Tunable charge transfer dynamics at tetracene/LiF/C₆₀ interfaces, *J. Phys. Chem. C* **119**, 1286 (2015).
- [13] Y. L. Huang, Y. J. Zheng, Z. B. Song, D. Z. Chi, A. T. S. Wee, and S. Y. Quek, The organic-2D transition metal dichalcogenide heterointerface, *Chem. Soc. Rev.* **47**, 3241 (2018).
- [14] H. M. Wang, C. H. Li, P. F. Fang, Z. L. Zhang, and J. Z. Zhang, Synthesis, properties, and optoelectronic applications of two-dimensional MoS₂ and MoS₂-based heterostructures, *Chem. Soc. Rev.* **47**, 6101 (2018).
- [15] S. H. Amsterdam, T. J. Marks, and M. C. Hersam, Leveraging molecular properties to tailor mixed-dimensional heterostructures beyond energy level alignment, *J. Phys. Chem. Lett.* **12**, 4543 (2021).
- [16] M. Gobbi, E. Orgiu, and P. Samori, When 2D materials meet molecules: Opportunities and challenges of hybrid organic/inorganic van der Waals heterostructures, *Adv. Mater.* **30**, 1706103 (2018).
- [17] L. Qin, B. Kattel, T. R. Kafle, M. Alamri, M. Gong, M. Panth, Y. Hou, J. Wu, and W. L. Chan, Scalable graphene-on-organometal halide perovskite heterostructure fabricated by dry transfer, *Adv. Mater. Interfaces* **6**, 1801419 (2019).
- [18] K. L. Zhang, Y. L. Feng, F. Wang, Z. C. Yang, and J. Wang, Two dimensional hexagonal boron nitride (2D-hBN):

- Synthesis, properties and applications, *J. Mater. Chem. C* **5**, 11992 (2017).
- [19] K. Nakano and K. Tajima, Organic planar heterojunctions: From models for interfaces in bulk heterojunctions to high-performance solar cells, *Adv. Mater.* **29**, 1603269 (2017).
- [20] K. Cnops, B. P. Rand, D. Cheyns, B. Verreet, M. A. Empl, and P. Heremans, 8.4% efficient fullerene-free organic solar cells exploiting long-range exciton energy transfer, *Nat. Commun.* **5**, 3406 (2014).
- [21] X. D. Chen, Z. B. Liu, C. Y. Zheng, F. Xing, X. Q. Yan, Y. S. Chen, and J. G. Tian, High-quality and efficient transfer of large-area graphene films onto different substrates, *Carbon* **56**, 271 (2013).
- [22] X. S. Li, Y. W. Zhu, W. W. Cai, M. Borysiak, B. Y. Han, D. Chen, R. D. Piner, L. Colombo, and R. S. Ruoff, Transfer of large-area graphene films for high-performance transparent conductive electrodes, *Nano Lett.* **9**, 4359 (2009).
- [23] B. Kattel, L. Qin, T. R. Kafle, and W. L. Chan, Graphene field-effect transistor as a high-throughput platform to probe charge separation at donor-acceptor interfaces, *J. Phys. Chem. Lett.* **9**, 1633 (2018).
- [24] S. Wanigasekara, B. Kattel, F. Rudayni, and W. L. Chan, Extracting electrons from delocalized excitons by flattening the energetic pathway for charge separation, *J. Phys. Chem. Lett.* **12**, 9047 (2021).
- [25] T. Wang, T. R. Kafle, B. Kattel, Q. F. Liu, J. Wu, and W. L. Chan, Growing ultra-flat organic films on graphene with a face-on stacking via moderate molecule-substrate interaction, *Sci. Rep.* **6**, 28895 (2016).
- [26] R. V. Gorbachev, I. Riaz, R. R. Nair, R. Jalil, L. Britnell, B. D. Belle, E. W. Hill, K. S. Novoselov, K. Watanabe, T. Taniguchi, A. K. Geim, and P. Blake, Hunting for monolayer boron nitride: Optical and Raman signatures, *Small* **7**, 465 (2011).
- [27] R. J. Koch, J. Katoch, S. Moser, D. Schwarz, R. K. Kawakami, A. Bostwick, E. Rotenberg, C. Jozwiak, and S. Ulstrup, Electronic structure of exfoliated and epitaxial hexagonal boron nitride, *Phys. Rev. Mater.* **2**, 074006 (2018).
- [28] D. R. T. Zahn, G. N. Gavrila, and M. Gorgoi, The transport gap of organic semiconductors studied using the combination of direct and inverse photoemission, *Chem. Phys.* **325**, 99 (2006).
- [29] W. Y. Gao and A. Kahn, Electronic structure and current injection in zinc phthalocyanine doped with tetrafluorotetracyanoquinodimethane: Interface versus bulk effects, *Org. Electron.* **3**, 53 (2002).
- [30] W. Chen, H. Huang, S. Chen, Y. L. Huang, X. Y. Gao, and A. T. S. Wee, Molecular orientation-dependent ionization potential of organic thin films, *Chem. Mater.* **20**, 7017 (2008).
- [31] S. Duhm, G. Heimel, I. Salzmann, H. Glowatzki, R. L. Johnson, A. Vollmer, J. P. Rabe, and N. Koch, Orientation-dependent ionization energies and interface dipoles in ordered molecular assemblies, *Nat. Mater.* **7**, 326 (2008).
- [32] M. Schwarze, K. S. Schellhammer, K. Ortstein, J. Benduhn, C. Gaul, A. Hinderhofer, L. P. Toro, R. Scholz, J. Kublitski, S. Roland, M. Lau, C. Poelking, D. Andrienko, G. Cuniberti, F. Schreiber, D. Neher, K. Vandewal, F. Ortmann, and K. Leo, Impact of molecular quadrupole moments on the energy levels at organic heterojunctions, *Nat. Commun.* **10**, 2466 (2019).
- [33] M. Iannuzzi, F. Tran, R. Widmer, T. Dienel, K. Radican, Y. Ding, J. R. Hutter, and O. Groning, Site-selective adsorption of phthalocyanine on *h*-BN/Rh(111) nanomesh, *Phys. Chem. Chem. Phys.* **16**, 12374 (2014).
- [34] F. Schulz, R. Drost, S. K. Hamalainen, and P. Liljeroth, Templated self-assembly and local doping of molecules on epitaxial hexagonal boron nitride, *ACS Nano* **7**, 11121 (2013).
- [35] See the Supplemental Material at <http://link.aps.org/supplemental/10.1103/PhysRevApplied.18.014042> for additional TRTPPE data, method for estimating exciton energy, and optical transfer-matrix model, which also includes Refs. [51–57].
- [36] T. Wang, Q. F. Liu, C. Caraiani, Y. P. Zhang, J. Wu, and W. L. Chan, Effect of Interlayer Coupling on Ultrafast Charge Transfer from Semiconducting Molecules to Mono- and Bilayer Graphene, *Phys. Rev. Appl.* **4**, 014016 (2015).
- [37] T. Wang and W. L. Chan, Dynamical localization limiting the coherent transport range of excitons in organic crystals, *J. Phys. Chem. Lett.* **5**, 1812 (2014).
- [38] M. K. L. Man, J. Madeo, C. Sahoo, K. C. Xie, M. Campbell, V. Pareek, A. Karmakar, E. L. Wong, A. Al-Mahboob, N. S. Chan, D. R. Bacon, X. Zhu, M. M. M. Abdelrasoul, X. Q. Li, T. F. Heinz, F. H. da Jornada, T. Cao, and K. M. Dani, Experimental measurement of the intrinsic excitonic wave function, *Sci. Adv.* **7**, eabg0192 (2021).
- [39] M. P. Seah and W. A. Dench, Quantitative electron spectroscopy of surfaces: A standard data base for electron inelastic mean free paths in solids, *Surf. Interface Anal.* **1**, 2 (1979).
- [40] Y. Ozawa, Y. Nakayama, S. Machida, H. Kinjo, and H. Ishii, Maximum probing depth of low-energy photoelectrons in an amorphous organic semiconductor film, *J. Electron. Spectrosc. Relat. Phenom.* **197**, 17 (2014).
- [41] T. R. Kafle, B. Kattel, T. Wang, and W.-L. Chan, The relationship between the coherent size, binding energy and dissociation dynamics of charge transfer excitons at organic interfaces, *J. Phys.: Condens. Matter* **30**, 454001 (2018).
- [42] L. Qin, L. P. Wu, B. Kattel, C. H. Li, Y. Zhang, Y. B. Hou, J. Wu, and W. L. Chan, Using bulk heterojunctions and selective electron trapping to enhance the responsivity of perovskite-graphene photodetectors, *Adv. Funct. Mater.* **27**, 1704173 (2017).
- [43] A. Laturia, M. L. Van de Put, and W. G. Vandenberghe, Dielectric properties of hexagonal boron nitride and transition metal dichalcogenides: From monolayer to bulk, *npj 2D Mater. Appl.* **2**, 6 (2018).
- [44] K. Noori, N. L. Q. Cheng, F. Y. Xuan, and S. Y. Quek, Dielectric screening by 2D substrates, *2D Mater.* **6**, 035036 (2019).
- [45] A. Raja, A. Chaves, J. Yu, G. Arefe, H. M. Hill, A. F. Rigosi, T. C. Berkelbach, P. Nagler, C. Schuller, T. Korn, C. Nuckolls, J. Hone, L. E. Brus, T. F. Heinz, D. R. Reichman, and A. Chernikov, Coulomb engineering of the bandgap and excitons in two-dimensional materials, *Nat. Commun.* **8**, 15251 (2017).
- [46] G. Konstantatos, M. Badioli, L. Gaudreau, J. Osmond, M. Bernechea, F. P. G. de Arquer, F. Gatti, and F. H. L.

- Koppens, Hybrid graphene-quantum dot phototransistors with ultrahigh gain, *Nat. Nanotechnol.* **7**, 363 (2012).
- [47] Y. B. Zhang, T. T. Tang, C. Girit, Z. Hao, M. C. Martin, A. Zettl, M. F. Crommie, Y. R. Shen, and F. Wang, Direct observation of a widely tunable bandgap in bilayer graphene, *Nature* **459**, 820 (2009).
- [48] J. B. Oostinga, H. B. Heersche, X. L. Liu, A. F. Morpurgo, and L. M. K. Vandersypen, Gate-induced insulating state in bilayer graphene devices, *Nat. Mater.* **7**, 151 (2008).
- [49] S. M. Falke, C. A. Rozzi, D. Brida, M. Maiuri, M. Amato, E. Sommer, A. De Sio, A. Rubio, G. Cerullo, E. Molinari, and C. Lienau, Coherent ultrafast charge transfer in an organic photovoltaic blend, *Science* **344**, 1001 (2014).
- [50] A. A. Bakulin, A. Rao, V. G. Pavelyev, P. H. M. van Loosdrecht, M. S. Pshenichnikov, D. Niedzialek, J. Cornil, D. Beljonne, and R. H. Friend, The role of driving energy and delocalized states for charge separation in organic semiconductors, *Science* **335**, 1340 (2012).
- [51] C. C. Katsidis and D. I. Siapkas, General transfer-matrix method for optical multilayer systems with coherent, partially coherent, and incoherent interference, *Appl. Opt.* **41**, 3978 (2002).
- [52] B. Harbecke, Coherent and incoherent reflection and transmission of multilayer structures, *Appl. Phys. B: Photophys.* **39**, 165 (1986).
- [53] S. J. Byrnes, Multilayer optical calculations, [arXiv:1603.02720v2](https://arxiv.org/abs/1603.02720v2) (2016).
- [54] M. Friedrich, T. Wagner, G. Salvan, S. Park, T. U. Kampen, and D. R. T. Zahn, Optical constants of 3,4,9,10-perylenetetracarboxylic dianhydride films on silicon and gallium arsenide studied by spectroscopic ellipsometry, *Appl. Phys. A: Mater.* **75**, 501 (2002).
- [55] S. Cheon, K. D. Kihm, H. G. Kim, G. Lim, J. S. Park, and J. S. Lee, How to reliably determine the complex refractive index (RI) of graphene by using two independent measurement constraints, *Sci. Rep.* **4**, 6364 (2014).
- [56] H. J. Lee, C. H. Henry, K. J. Orlowsky, R. F. Kazarinov, and T. Y. Kometani, Refractive-index dispersion of phosphosilicate glass, thermal oxide, and silicon-nitride films on silicon, *Appl. Opt.* **27**, 4104 (1988).
- [57] D. E. Aspnes and A. A. Studna, Dielectric functions and optical-parameters of Si, Ge, GaP, GaAs, GaSb, InP, InAs, and InSb from 1.5 to 6.0 eV, *Phys. Rev. B* **27**, 985 (1983).